Photostimulated desorption of OH radicals from amorphous solid water: Evidence for the interaction of visible light with an OH-ice complex

A. Miyazaki,[1] N. Watanabe ⬤,[1,*] W. M. C. Sameera ⬤,[1] Y. Nakai ⬤,[2] M. Tsuge ⬤,[1] T. Hama ⬤,[1,3]
H. Hidaka ⬤,[1] and A. Kouchi ⬤[1]

[1]*Institute of Low Temperature Science, Hokkaido University, N19-W8, Kita-ku, Sapporo, Hokkaido 060-0819, Japan*
[2]*Radioactive Isotope Physics Laboratory, RIKEN Nishina Center, Wako, Saitama 351-0198, Japan*
[3]*Komaba Institute for Science, The University of Tokyo, 3-8-1 Komaba, Meguro, Tokyo 153-8902, Japan*

Using a combination of photostimulated desorption and resonance-enhanced multiphoton ionization techniques, OH radicals photodesorbed from amorphous solid water at low temperatures are detected. It was found that the OH photodesorption can be caused by a one-photon process on the surface even at 532 nm, where both isolated OH and H_2O are transparent. Quantum chemical calculations reveal that the electronic excitation of OH dramatically changes depending on the adsorption sites and the number of surrounding H_2O molecules, and that OH having three hydrogen bonds with neighboring H_2O molecules can absorb photons of around 532 nm, which supports the experimental findings.

I. INTRODUCTION

The behavior of hydroxyl (OH) radicals on water ice is closely related to various phenomena occurring on ice-dust particles in atmospheric and interstellar environments. In interstellar molecular clouds, which are located in very cold regions of space, the OH radical is considered to be one of the dominant species on cosmic ice dust, because it can be readily produced by photolysis of H_2O on ice, as well as by reactions of hydrogen and oxygen, which are abundant elements in space [1,2]. When OH radicals have accumulated on the ice-dust surface, they play a key role in the production of various interstellar molecules, such as CO_2, H_2O_2, and HCOOH [3]. Even at temperatures as low as 10 K, the reactions of OH radicals were found to occur on the ice surface through low-barrier, barrierless, or tunneling reactions [4–6]. Therefore, the previous experiments mainly concentrated on the reactions of OH on amorphous solid water (ASW), which is an analog of cosmic ice dust. Those were performed mainly by spectroscopically measuring stable molecular products on ice and thus it is not yet clear how OH radicals themselves behave on the ice surface. To better understand the physicochemical processes of OH radicals on ice, close monitoring of the radicals is crucial. However, the detection of OH has intrinsic experimental difficulties. Since OH radicals easily react with one another or an adsorbate, it is difficult to produce sufficient amounts of OH on ice for detection with the conventional methods. Furthermore, spectroscopic separation of OH radicals on the surface from those in bulk ice is fraught with problems. Therefore, methods often used for solids, such as Raman, infrared, and electron spin resonance spectroscopies, are not applicable. Microscopic methods, such as scanning tunneling microscopy and field-emission microscopy, can de-

tect adsorbates on the surface [7–9], but these methods are inappropriate to distinguish between OH and H_2O. Furthermore, ice is not an electric conductor. Recently, OH radicals in bulk ice were detected by near-edge x-ray absorption fine-structure spectroscopy, but unfortunately, this method is not surface sensitive [10,11].

Complementing the experimental approach, calculations have mainly treated OH interacting with H_2O clusters. The binding energies of OH radicals and H_2O clusters were determined by calculations [12–14]. Most recently, quantum chemical calculations have provided several binding energies for OH on crystalline ice, depending on adsorption sites, in the range 0.20–0.67 eV [15]. There is no report on binding energies for OH radicals on the ASW surfaces. Furthermore, it is difficult to predict the binding-site distribution of ice, and therefore an experimental approach is still desirable.

Recently, we developed a method to sensitively detect atomic hydrogen on the ice surface with a combination of photostimulated desorption (PSD) at 532 nm and resonance-enhanced multiphoton ionization (REMPI) techniques [16,17]. In the present paper, we report the detection of OH radicals produced by photolysis of ASW deposited on an aluminum substrate at low temperatures by the PSD-REMPI method. Because neither an isolated OH radical nor an H_2O molecule absorbs a photon at 532 nm, mechanisms causing PSD of OH need to be thoroughly discussed. From analyzing the obtained translational energy of photodesorbed OH radicals and quantum chemical calculations, we propose that the PSD process is triggered by the absorption of a photon at 532 nm by an OH radical that has three hydrogen bonds with H_2O molecules on the ASW surface.

II. EXPERIMENT

Samples of nonporous ASW, with the thicknesses from about 20 to 1000 monolayers (MLs), were produced at 100 K

by vapor deposition of H_2O gas from freeze-pump-thaw cycled ultrapure water (>18 MΩ cm) on a mirror-polished aluminum substrate (40 mm in diameter) connected to the cold head of a He refrigerator. The aluminum surface was cleaned up neither by heating nor by ion bombardments in the vacuum. Therefore, the surface should be oxidized to some extent. The OH radicals were produced by UV photolysis of ASW. The sample temperature upon ultraviolet (UV) irradiation was in the range from 10 to 80 K. Since temperature barely influenced the results, we focus on the experiments conducted at 70 K. The UV photons were emitted from a conventional deuterium UV lamp (H2D2 light source unit, Hamamatsu Photonics K. K.) in the wavelength range of 115–400 nm, and were then collimated by a capillary plate to illuminate only the ASW sample. This device avoids the creation of undesired photoelectrons from the metal surfaces of the chamber wall and the cold head. The UV flux (approximately 1×10^{13} photons $cm^{-2} s^{-1}$) was measured by a photodiode (AXUV-100G, IRD Inc.) above the sample surface. The threshold of the first electronic excited state of H_2O, which is dissociative, is around 7.3 eV (170 nm) [18]. The photons from the UV lamp dissociate H_2O molecules, mainly into H + OH [19]. Possible photoproducts, H, H_2, O, and O_2, other than OH cannot stay on the surface at 70 K. For the same type of UV lamp, the effective cross section of photoabsorption by H_2O ice over the whole wavelength range was reported to be 3.4×10^{-18} cm^2 [20]. In the present experiments, the OH measurements by the PSD-REMPI method were mostly started after about 1 h of UV exposure when the OH intensity became constant at a steady state. If all of the photoproduced OH remains on the surface, the surface coverage of OH can reach about 0.1 on the assumption that photoabsorption always leads to photodissociation. Furthermore, an amount of tens of percent for the OH photoyields was reported to desorb immediately [20]. Most importantly, we found that our detected OH yields over 1 min exposure reached a similar level within a factor of 2 to those over 1 h at the steady state. Because the exposure time of 1 min provides the coverage of 0.002 at a maximum, the desorption process needs to happen under the condition that OH radicals are almost isolated on a pure H_2O surface. This quick saturation of OH yields was also seen in the experiments by Cruz-Diaz *et al.* [20], where they measured the OH photodesorption yields during exposure of ice to UV from a deuterium lamp. These findings indicate that the surface number density of OH is settled in the steady state by the balance between photoproduction and loss by photodesorption and recombination such as OH + OH → H_2O_2 or H_2O + O [4,21]. H_2O_2 would reproduce two OH radicals by UV. These products may desorb at the formation reaction [22,23]. Experiments were conducted in an ultra-high vacuum chamber with the pressure lower than 2×10^{-7} Pa under UV irradiation. Main contamination on the ASW surface at 70 K would be CO_2 (mass 44), and the deposition rate of CO_2 is estimated to be 1.9% of coverage per hour. This contamination level would not affect the experiments conducted within 1–2 h.

During continuous UV exposure, OH radicals on the surface of ASW are photodesorbed by weak nanosecond laser radiation (typically 40 μJ per pulse on an approximate 3 mm^2 spot) at 532 nm (hereafter denoted as a PSD laser). The in-
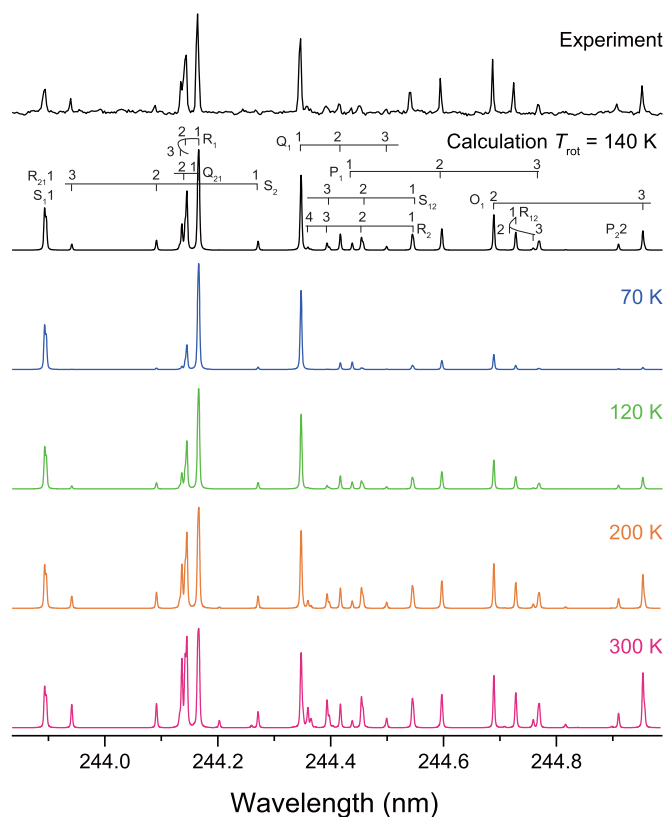

FIG. 1. (2+1) REMPI spectra of OH obtained in the experiment (top) and simulation calculation for OH in the transition of $D\,^2\Sigma^-\,(v'=0) \leftarrow X\,^2\Pi(v''=0)$ with a rotational temperatures of 70–300 K using the PGOPHER program (lower). Although the spectrum at 140 K best reproduces the experiment, those at 120 and 200 K also fit that fairly well. The experimental spectrum was acquired for the higher translational energy component which is discussed in Sec. III.

cident angle was ca. 45 ° with respect to the surface normal and the polarization to the plane of incidence was parallel (p polarized). After a given delay to the PSD laser shot, the photodesorbed OH radical is selectively ionized by another laser radiation for the REMPI process at about 1 mm above the ASW surface, and mass analyzed using a time-of-flight method for which the aluminum substrate served as the first electrode. From the delay and distance between the focal point of the REMPI laser and the surface, the translational energy distribution of photodesorbed OH radicals can be determined. The REMPI laser wavelength was tuned in the range for the transition, $D\,^2\Sigma^- \leftarrow X\,^2\Pi$ [24]. Figure 1 shows a (2+1) REMPI spectrum of OH obtained from the surface of UV-photolyzed ASW at 70 K, together with a simulation calculation by the PGOPHER program [25] with molecular constants reported in the literature [26,27]. As shown in Fig. 1, the simulation of an OH radical in the transition $D\,^2\Sigma^- \leftarrow X\,^2\Pi$, with rotational temperatures approximately from 120 to 200 K, reproduces the obtained spectrum fairly well. Without UV exposure, OH radicals were not observed but only H_2O molecules were detected by the PSD-REMPI method (see Fig. 2). The PSD-REMPI spectra of H_2O were obtained regardless of the UV exposure. The
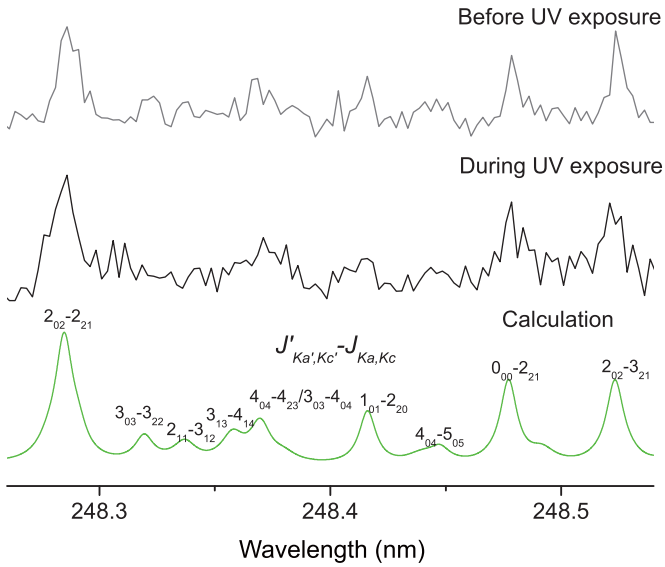
FIG. 2. PSD-REMPI spectra of H_2O obtained before (top) and during (middle) UV exposure of ASW at 70 K with simulation by PGOPHER for the rotational temperatures of 140 K (bottom). The experimental spectra are reproduced fairly well by calculations for rotational temperatures from 120 to 200 K. Notations, $J'_{Ka',Kc'}$–$J_{Ka,Kc}$, are rotational assignments in the two-photon $\tilde{C}\,^1B_1(v'=0, J'_{Ka',Kc'})$–$\tilde{X}\,^1A_1(v''=0, J_{Ka,Kc})$ transition of H_2O.

PSD-REMPI intensities of OH radicals were approximately proportional to the square of REMPI laser power, indicating that the PSD-(2+1) REMPI method works for the detection of OH on ice. The PSD-REMPI spectral pattern was found to be independent of ASW temperature. Although the rotational temperature should be certainly affected by photodesorption dynamics, the mechanism for determining the rovibrational population is not clear. This kind of independence of rotational temperature has also been reported in the experiment on H_2O photodesorption from ice [28]. In contrast, the rotational temperature of CH_3 directly desorbed from

photofragmentation of solid CH_3OH has been reported to be thermalized at the solid temperature, suggesting desorption following bulk diffusion [29]. Here it should be noted that, unlike previous experiments [28,29], in the present experiment the OH production by the UV photolysis did not coincide with the OH desorption caused by the PSD laser shot. Therefore, most of the detected OH radicals would have already lost the energies initially gained upon the UV photodissociation. If our detected OH radicals originate from the underlayer H_2O in bulk ice, the rotation of OH might be thermalized at the ice temperature during bulk-diffusive desorption. Therefore, we deduce that the PSD-REMPI signals originate from OH adsorbates at the top of the surface, and not from OH in the underlayers as described later.

III. EXPERIMENTAL RESULTS AND DISCUSSSION

The detected OH intensities reflect the surface number densities of OH, which are determined by the balance between OH production by UV photolysis and OH loss by photodesorption and/or diffusive OH-OH recombination to produce $H_2O + O$ or H_2O_2. As mentioned above, the detected OH intensities were almost independent of the temperature below 80 K. Furthermore, the OH intensities were obtained for a steady-state condition, where they were time independent. We found that, at temperatures above 80 K, the OH intensities diminished significantly probably due to the recombination and/or desorption. Hereafter, the REMPI intensity is represented by peak area intensity for the $R_1(J=1)$ branch (244.164 nm) of the $D\,^2\Sigma^- \leftarrow X\,^2\Pi$ transition. We confirmed that the REMPI intensity was not saturated, and increased with the PSD laser intensity.

Figure 3(a) shows the variation in REMPI signal intensity as a function of delay time; the observed profile is directly correlated with the translational energy distribution of photodesorbed OH (hereafter, referred to simply as translational energy distribution). Using the same manner as described previously [30], the profiles can be fitted well by flux-weighted Maxwell-Boltzmann distributions with two components of
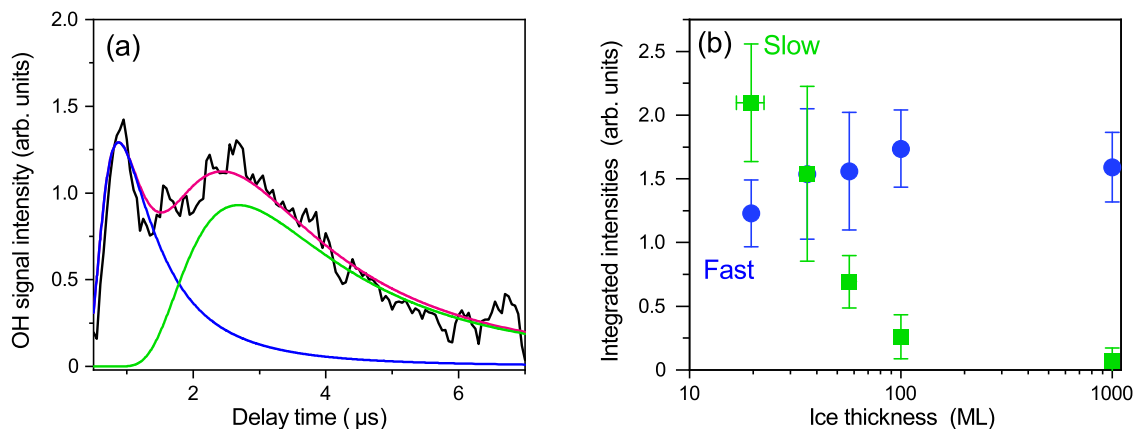

FIG. 3. (a) Translational energy distribution of OH photodesorbed. Black line represents the five points adjacent averages of the obtained OH REMPI intensities. Red line is a fit to the data with two-component Boltzmann distribution at 3000 and 320 K for faster (blue filled circles) and slower (green squares) components. (b) Ice thickness dependence of faster- and slower-component intensities. Each intensity was derived by integration of Boltzmann-fitted curve [blue or green curve in (a)].
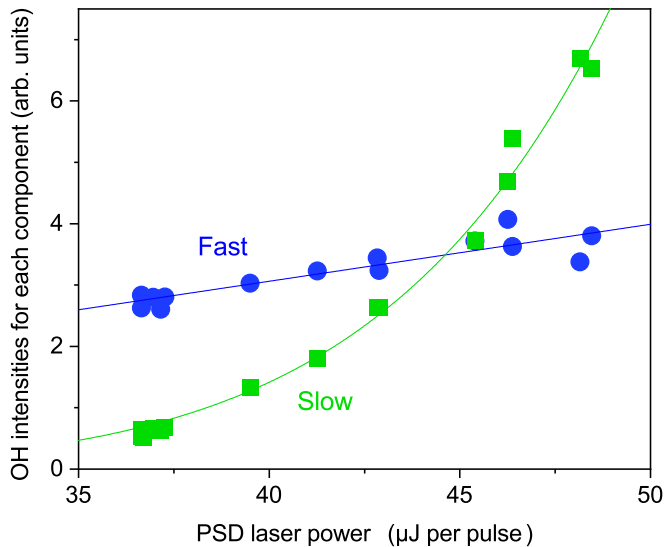
FIG. 4. The PSD laser power dependence of integrated intensities for the Boltzmann fitted faster (blue filled circles) and slower (green squares) components. Solid lines are fits according to $y = ax^b$. The data plots for the faster and slower components are best fitted by linear where $b = 1.21 \pm 0.14$ and power-of-8 relations, respectively.

about 3000 ± 600 K and 320 ± 70 K (corresponding to approximately 0.26 ± 0.05 eV and 0.027 ± 0.006 eV, respectively), which are independent from ASW temperature. Uncertainties mainly arise from errors in the measurement of the distance from the surface to the focal point. The obtained Maxwell-Boltzmann distributions do not necessarily mean that the photodesorption occurs at thermally equilibrated sites. In fact, the obtained rotational and translational temperatures are not consistent. It is known that the velocity distributions of molecules desorbed by nonthermal mechanisms in many cases also closely resemble thermal distributions, although translational temperatures obtained from fits to Maxwellians do not seem to be related to surface temperature [31]. In any case, it is difficult to explain this higher translational temperature (faster component) by laser-induced thermal desorption, while the lower translational temperature (slower component) may be attributed to gentle desorption such as phonon-mediated desorption suggested previously for the PSD of H atoms from ASW [17]. The translational energies of phonon-mediated desorbed molecules by laser irradiation were reported to be below ~ 0.1 eV [32,33].

To clarify the desorption mechanism, the dependence of intensity on ice thickness was measured for each component. If the desorption results from a photochemical process at the ice surface, the intensity should only weakly depend on ASW thickness. On the other hand, if the desorption is caused by a substrate-mediated process such as phonon propagation, intensity should decrease as thickness increases. In our previous PSD-REMPI measurements, where H atoms on ASW were detected, a photodesorption process was proposed to occur by phonon propagation from the substrate, rather than a photochemical process on the surface [17]. As seen in Fig. 3(b), the thickness dependences of the faster and slower components accord with the expected behaviors of desorption by the photochemical and phonon-mediated processes, respec-

tively. The intensity of the faster component slightly increases with thickness, which can be attributed to the ASW surface area tending to increase with thickness [34]. Furthermore, we confirmed that the intensity for the faster component is proportional to PSD laser power as consistent with one-photon chemical processes (see Fig. 4). However, it should be noted that neither isolated H_2O, OH, nor H_2O-OH binary have an absorption band at around 532 nm. In contrast, the intensity of the slower component strongly depends on the thickness of ASW [Fig. 3(b)] and shows a power-law dependence on laser power (Fig. 4). Although the meaning of the specific number of order is unclear, the phonon-mediated desorption was reported to show a power-law dependence on energy input to the surface [35]. The phonon-mediated desorption should work only for OH weakly bonded on the ASW surface. Such OH adsorbates may thermally migrate to stronger adsorption sites relatively easily. To support this scenario, we performed additional experiments, where OH radicals were detected after switching off the UV lamp. In this measurement, the slower component diminished significantly while the faster component remained [see Fig 5(a)]. The slower component is only detectable when OH is produced continuously. This implies that weakly bonded OH radicals easily leave sites, leading to trapping in deeper potential sites, OH-OH recombination, and/or desorption, while strongly bonded OH radicals remain at the same sites, even after UV termination. As mentioned in Sec. II, we also detected H_2O desorbed from the ASW surface by the PSD-REMPI method (see Fig. 2). By monitoring the peak at 248.285 nm (2_{02}–2_{21} transition) with changing the delay between the PSD and REMPI laser shot, the translational energy distribution of H_2O was obtained as shown in Fig. 5(b). The distribution has only the slower component with the translational energy corresponding to about 300 K, which is consistent with that for OH. The profile of the spectra remains unchanged between the UV irradiation on and off. Furthermore, the PSD-REMPI intensity of H_2O became weaker with increase of thickness, similarly to the slower component of OH. At the same time, it becomes clear that the desorption process for the faster component is specific for OH.

Before further discussing the desorption mechanisms, the other photoprocesses that may trigger the OH desorption should be considered. One possible mechanism that deserves evaluation is related to electrons emitted from metal surfaces. When water ice on metal surfaces is exposed to photons at energies even below work functions of metals, the hot electrons are known to be emitted from the metal to ice as solvated electrons; when solvated electrons are trapped on the surface of ice, its lifetime can become on the order of seconds or more. This process was investigated by time-resolved two-photon photoelectron spectroscopy, where pump laser irradiation created the hot electrons and a subsequent probe laser further excited them into the vacuum [36,37]. Some of these electrons were found to be stabilized in the ice-vacuum interface for a long time, up to about 100 s, depending on morphology and thickness of ice [36,37]. Such long-lived electrons might induce processes leading to the desorption of OH. We first discuss the possibility of photodesorption triggered by the hot electrons. In the present experiment, two kinds of photon sources were used: the cw deuterium lamp and a nanosecond
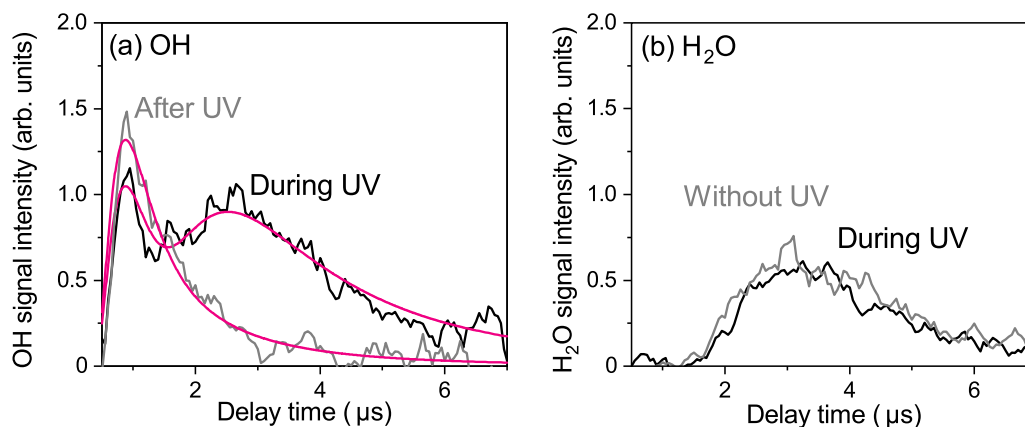
FIG. 5. (a) Translational energy distribution of OH obtained during (black line) and after (gray line) UV irradiation. Red lines are fits using a Boltzmann distribution. The spectrum during UV irradiation is best fitted by the faster and slower two-component distribution while that after UV irradiation is reproduced only by the faster component. (b) Translational energy distribution of H_2O obtained during UV irradiation (black line) and without UV exposure (gray line). The intensities of H_2O after UV exposure are consistent with those without UV.

laser at 532 nm. The photons at 532 nm cannot work as a pump light for the hot electrons because the photon energy does not reach the conduction band of ice, where the hot electrons are stabilized and long lived. The UV photons from the deuterium lamp may produce solvated electrons in ASW from the aluminum substrate. In order to examine the influence of long-lived electrons which might exist at the ASW surface, we performed an additional experiment as follows. The ASW samples were left for a given time period after turning the UV light off. Even after tens of minutes, the OH radicals were still detected at the delay time for the peak of the faster component by the PSD-REMPI methods (see Fig. 6). The time gap between the PSD-REMPI measurements and the UV termination, where the OH was detected, obviously exceeds the lifetime of long-lived electrons reported for ASW [36,37]. Furthermore, the variation of OH intensities with time delay
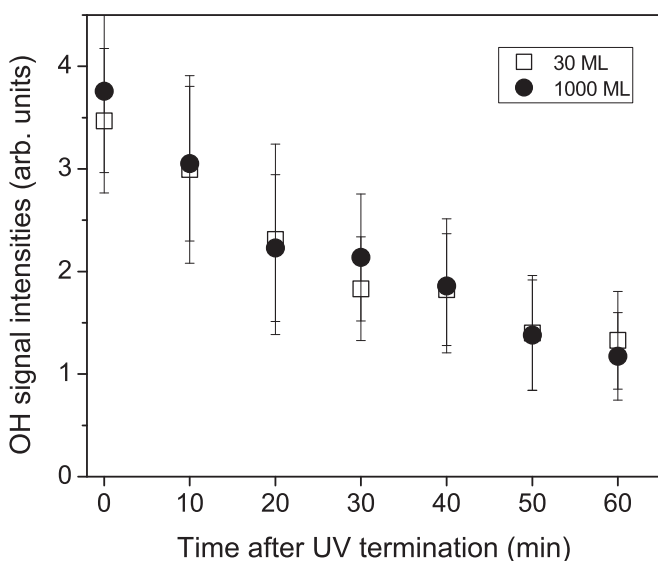

FIG. 6. The PSR-REMPI intensities for OH at the peak of faster component after the termination of UV irradiation. The PSD laser irradiation was operated only every 10 min at detection.

was found to be independent of the ASW thickness whereas the lifetime of solvated electrons is reported to depend on the thickness. Therefore, we conclude that the hot electron process would not play a role in the desorption of OH.

Another possible desorption process would be plasmon-stimulated desorption. When a surface plasmon is excited on metal surfaces by laser irradiation under appropriate condition, the desorption of molecular adsorbates together with the metal atoms is observed [38–40]. For example, desorption of dye molecules from the aluminum surface was observed by the laser irradiation at 532 nm [39]. Desorption of sodium atoms from Na nanoparticles was reported and the desorption rate was found to depend linearly on the light intensity [38]. However, the surface-plasmon excitation with visible light requires a specific correlation between wavelength and surface geometry of metals. That is, the plasmon-induced desorption was only observed from metal nanoparticles or laser injection in an attenuated total reflection geometry at specific angles. These conditions do not match the present experiment. In addition, thickness independence of the faster component up to $\sim$1000 MLs shown in Fig. 3(b) would hardly be explained by the hot electron or plasmon processes. As a result, the hot electrons and surface-plasmon excitation can be ruled out as the desorption mechanism of OH in our experiment.

In addition, in order to more directly exclude the possibility that electrons in the metal cause the desorption of OH, we performed the identical experiments with ASW deposited on a substrate of sapphire crystal which is almost transparent for photons at 532 nm. A sapphire disk with a thickness of 0.5 mm and a diameter of 6 mm was mounted at the center of the original aluminum substrate with a diameter of 40 mm. Although sapphire is an insulator, this concentric arrangement of aluminum and small sapphire disks enables the time-of-flight measurements. Figure 7(a) shows the translational energy distribution of OH photodesorbed from the ASW deposited on the sapphire substrate. One can see the profile exhibits the single faster component which can be fitted by the Boltzmann distribution at 2960 $\pm$ 180 K which is consistent with the faster component shown in Fig 3(a). The absence of the slower component would be reasonable because the photons
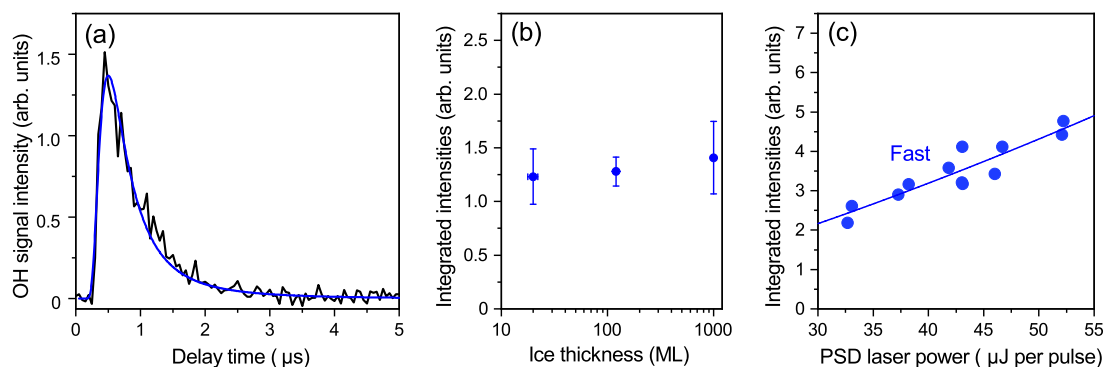
FIG. 7. (a) Translational energy distribution of OH photodesorbed from ASW deposited on the sapphire substrate during UV exposure. Black line represents the five points adjacent averages of the obtained OH REMPI intensities. The blue line represents a fit of data to a single Boltzmann distribution at 2960 ± 180 K. The ice thickness (b) and the PSD power (c) dependences of OH intensities obtained from ASW deposited on the sapphire disk. The solid line in (c) represents linear fitting of the data.

at 532 nm interact little with the sapphire crystal. The ice thickness and PSD laser power dependences are consistent with those for the faster component of OH desorbed from the ASW deposited on the aluminum surface [see Figs. 7(b) and 7(c)]. As a result, we conclude that the faster component originates from the interaction between a single photon at 532 nm and OH at the top layers of ASW and that electrons from metals play a negligible role. In order to get more insights about the OH radical behavior on ice, we performed quantum chemical calculations.

IV. COMPUTATIONAL METHODS

Ice cluster models for hexagonal ice crystal (ice I_h) or ASW (Fig. 8) were fully optimized using the two-layer our own *N*-layer integrated molecular orbital molecular mechanics (ONIOM) method [41,42] implemented in the GAUSSIAN16 program [43]. In this method, a quantum mechanical (QM) approach is applied for the electronically important part of the molecular system, while a molecular mechanics (MM) approach is used for the remaining part. In the ASW ice cluster model A shown in Fig. 8, 46 water molecules are in the high layer, and 113 water molecules are in the low layer. For ice I_h cluster models B and C (Fig. 8), three water layers were included. Ice cluster model B consists of 48 water molecules in the ONIOM high layer, while the remaining 114 water molecules are in the ONIOM low layer. In the case of ice cluster model C, 44 water molecules are in the high layer, and 112 water molecules are in the low layer. In order to reduce the computational cost and to avoid structural deformation, water molecules at the bottom and sides of the cluster model were frozen upon structure optimization. The wB97X-D functional [44] and def2-TZVP basis sets [45] were employed for the high layer. The AMBER force field [46]
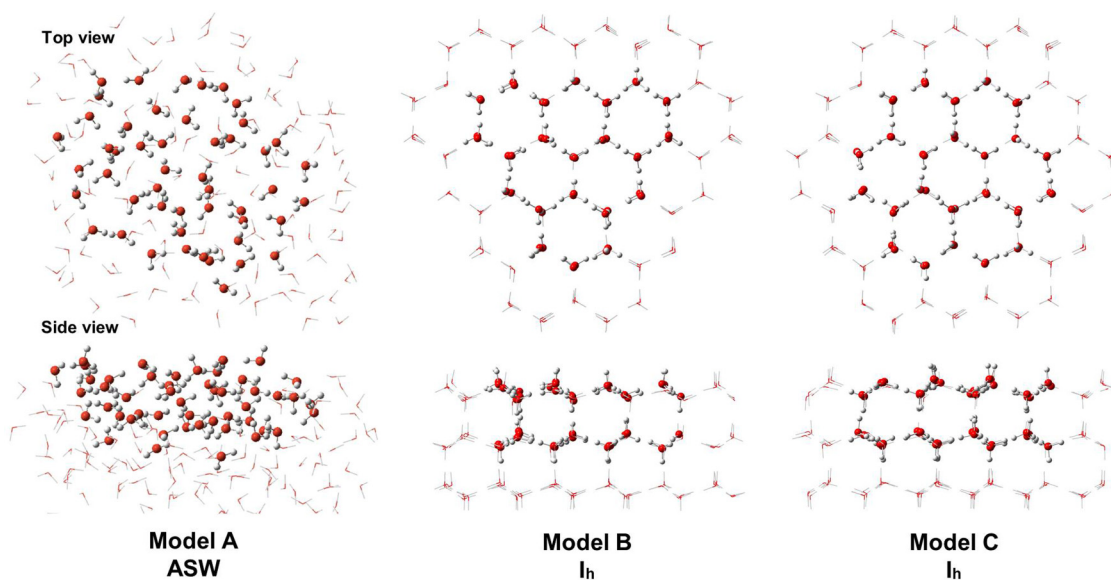

FIG. 8. Top and side views of the ice cluster models for amorphous solid water (ASW, model A) and for hexagonal ice crystal (ice I_h, models B and C). "Ball and sticks" show the high layer, and the "wire frame" shows the low layer.

was used for the low layer. Vibrational frequency calculations were performed to confirm that the optimized structures were minima (i.e., no imaginary frequencies), and to calculate zero-point energies. Vertical excitation energies were calculated using time-dependent density functional theory (TDDFT). The wB97X-D or M06-2X [47] functionals were used for the ONIOM high layer, as they have been performing well for excited-state calculations [48–50]. The def2-TZVP basis sets were employed. The "UltraFine" integration grid was used with the M06-2X functional. Conical intersection calculations were performed using the GRRM17 program [46].

V. COMPUTATIONAL RESULTS AND DISCUSSION

We first calculated the binding energies of OH radicals on 28 binding sites; 18 binding sites A1–A18 on the ASW surface, and ten sites B1–B3 and C1–C7 on the ice I_h surface, where the numbering was done arbitrarily. A range of binding energies (from 0.06 to 0.74 eV) was obtained, depending on the number of dangling-H or dangling-O atoms on the binding site. Assuming the calculated binding sites are equally distributed on the surface, the average binding energy is 0.37 eV. The binding energy becomes as weak as 0.06 eV when the OH radical does not interact with dangling atoms on ice. In such a case, we deduce that OH radicals can desorb by mild processes, such as the propagation of phonons from the aluminum substrate beneath the ice sample, without the direct photoabsorption by adsorbates. Such weakly bound OH radicals can be the origin of the slower component in the PSD-REMP spectra. When OH interacts with three water molecules through hydrogen bonds, binding energies as high as 0.74 eV are obtained. Strongly adsorbed OH radicals on ice cannot be desorbed through a mild thermal process. In order to gain some insight into the photochemical process, we studied the excited states of the OH radicals on the ice surface.

In the case of an isolated OH radical in the gas phase, there are two equivalent p orbitals perpendicular to the molecular axis, and therefore the ground state is a doubly degenerate $^2\Pi$ state [51]. Excitation to the first doublet excited state ($^2\Sigma^+$), i.e., the $^2\Sigma^+ \leftarrow {}^2\Pi$ valence transition localized on OH, the so-called A-X transition, occurs at 309 nm (4.0 eV). When an OH radical interacts with a water molecule (forming an H_2O-OH complex), the degeneracy of the $^2\Pi$ state can be lifted, giving rise to two low-lying hole states [52]. The energy splitting between these states is as small as ∼0.02 eV, which is confirmed by both experimental [53] and theoretical studies [54]. According to *ab initio* calculations [51], the computed vertical A-X transition of the H_2O-OH complex is red-shifted by about 0.4 eV compared with the A-X transition of an isolated OH radical. In the presence of several water molecules near the OH radical, interactions between the OH radical and H_2O molecules lead to a broad absorption band [55]. The red-shifted region of the absorption band originates from the valence transition localized on OH (i.e., the A-X transition). The A-X transition wavelengths for the OH radical bound ice cluster models calculated with the ONIOM(wB97X-D/def2-TZVP:AMBER) level of theory are plotted as a function of binding energy in Fig. 9.

In general, calculated A-X transitions are mainly in the region of 300–400 nm, and are in agreement with a previous
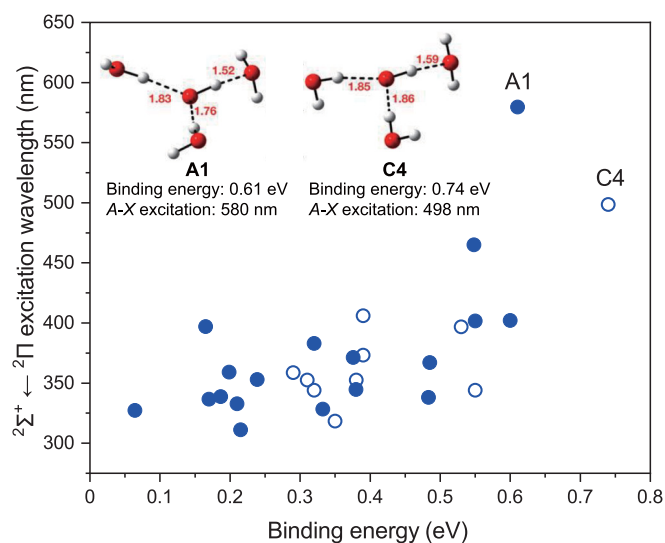

FIG. 9. Calculated $^2\Sigma^+ \leftarrow {}^2\Pi$ vertical excitation energy using wB97X-D functional in wavelength as a function of binding energy of an OH radical bound ice cluster model. Filled circles represent the data points calculated for amorphous ice surface (model A) and open circles for ice I_h (models B and C). The molecular structures of OH radicals at A1 and C4 binding sites are shown, where calculated binding energies are largest.

report [51]. At the present level of theory, using two of the best performing density functionals, the calculated $^2\Sigma^+ \leftarrow {}^2\Pi$ excitation can also occur around 500–600 nm, when the binding energy is very high (see binding sites A1 and C4 in Fig. 9). Very high binding energies originate from the three strong hydrogen bonds between a single OH radical and three water molecules on the ice surface (see structures shown in Fig. 9). It should be noted that our calculated binding sites cannot cover those for OH on all of the possible ice structures which can change by ice preparation. In other words, it is not realistic to calculate all the possible structures. Although our calculated A-X excitations do not precisely match the photon energy of the PSD laser used in the experiment, OH at some binding sites can certainly absorb the photon at 532 nm because the A-X transition is very sensitive to the surface structure at the OH binding site.

For the verification of calculated vertical excitation wavelength, we investigated the effects of the chosen density functionals and the size of the QM region. In the ice cluster model A1, where 46 H_2O molecules are in the ONIOM high layer (i.e., QM region), the computed A-X excitation occurs at 580 and at 619 nm with the ONIOM(wB97X-D:AMBER) and ONIOM(M06-2X:AMBER) methods, respectively. The calculated vertical excitation energies for two different functionals are close to each other with the difference of 0.14 eV (less than 10% of vertical excitation energies). For ice cluster models A1–A18, an averaged difference was 0.22 ± 0.11 eV. In order to check whether the number of water molecules in the ONIOM high layer has an effect on the computed A-X excitation, we have calculated vertical excitation energies by changing the number of H_2O molecules in the ONIOM high layer of A1 and C4 binding sites (Fig. 10). Computed A-X excitations are sensitive to the number of H_2O
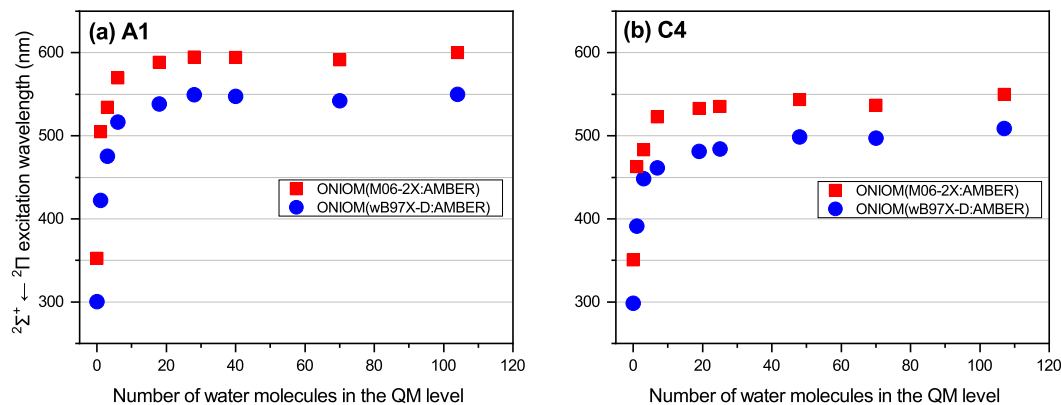
FIG. 10. (a) Computed *A-X* transition vs the size of the QM region for ASW model system A1. When the size of the QM region was increased, the vertical excitation wavelength converged to ∼550 nm with the ONIOM(wB97X-D:AMBER) method and ∼600 nm with the ONIOM(M06-2X:AMBER) method shown by blue dots and red square, respectively. (b) Computed *A-X* transition vs the size of the QM region for the ice I_h model system C4. Computed vertical excitation energy is converged when we increase the number of H_2O molecules in the ONIOM high layer.

molecules in the ONIOM high layer of the ice cluster models. When we increased the number of water molecules in the ONIOM high layer in ice cluster model A1, the computed *A-X* excitation wavelength increased, and converged to ∼550 and ∼600 nm with the ONIOM(wB97X-D:AMBER) and the ONIOM(M06-2X:AMBER) methods, respectively [Fig 10(a)]. Thus, the neighboring water molecules can lower the energy gap between the occupied and unoccupied orbitals of an OH radical on ice. We have observed a qualitatively similar picture for the ice cluster model C4 [see Fig. 10(b)].

Computed ground- and excited-state potential energy surfaces for an OH radical bound ice cluster model, using the wB97X-D/def2-TZVP level of theory, are shown in Fig. 11. In order to reduce the computational cost, a relatively small ice cluster model containing 19 H_2O molecules was used. The O atoms of the outermost H_2O molecules in the 19 H_2O cluster were frozen upon the structure optimizations to avoid structure deformations. The computed *A-X* transition is nearly converged when the QM region has about 19 H_2O molecules in either the ASW or the I_h models (Fig. 10). After the *A-X* transition, the excited-state geometry in the Franck-Condon region (FC) can be relaxed to the minimum of the second excited state (D_2), where the O(1)–H(1) bond is increased (1.41 Å). Once the system approaches the D_2 minimum, the OH cannot desorb if radiative decay brings the system into the ground state (D_0). We do not exclude this radiative decay without the desorption as one of relaxation channels. However, starting from the geometry of the D_2 minimum, we have located a conical intersection (CI) between the second and the third doublet excited-state potential energy surfaces, which is energetically similar to the D_2 minima. Thus, the excited-state structure at the D_2 minima can enter a dissociation channel through the CI, giving rise to the kinetic energy (KE) of 0.24 eV for OH, which is qualitatively in agreement with the translational energy of the faster component of the experimental translational energy distribution. Thus, the photodesorption of OH can be initiated by the *A-X* transition, and the subsequent desorption process would occur through a conical intersection near the D_2 minimum.

Our experiments and calculations first indicate that the OH desorption can be triggered by visible one-photon absorption of the OH-$(H_2O)_n$ complex at the ice surface. The photoabsorption would occur at specific binding sites, where an OH radical interacts with three H_2O molecules through hydrogen bonding. In other words, there would be many binding sites on ice from which OH cannot be detected by the PSD-REMPI method using the 532-nm PSD laser. By changing the wavelength of the PSD laser, we will obtain further insights into the photoexcitation and photodesorption of OH in the visible region. The developed method can be applied for the further investigation on physicochemical processes of the surface OH, which is closely related to chemical evolution on cosmic ice dust.
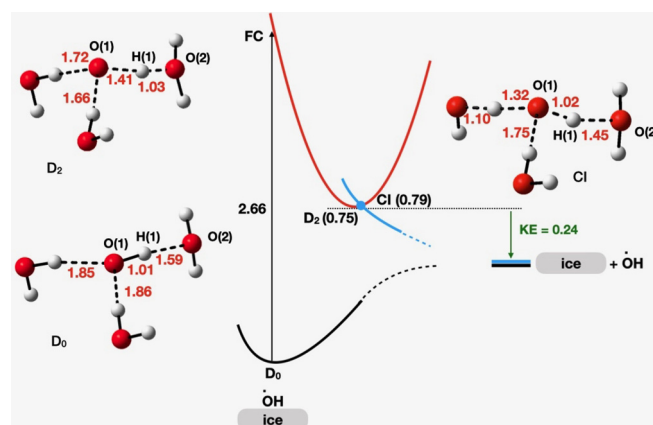

FIG. 11. Proposed mechanism for the photodesorption of OH radical on ice. D_0 and D_2 are local minima in the ground and second lowest excited states, respectively. The labels FC, CI, and KE denote Franck-Condon point, conical intersection, and kinetic energy, respectively. The energies are in eV and those in parentheses are relative to the D_0 minimum. The optimized local structures for D_0, D_2, and CI are shown with bond lengths in Å.

ACKNOWLEDGMENTS

[1] N. Watanabe and A. Kouchi, Prog. Surf. Sci. **83**, 439 (2008).

[2] T. Hama and N. Watanabe, Chem. Rev. **113**, 8783 (2013).

[3] R. T. Garrod, S. L. Widicus Weaver, and E. Herbst, Astrophys. J. **682**, 283 (2008).

[4] Y. Oba, N. Watanabe, A. Kouchi, T. Hama, and V. Pirronello, Phys. Chem. Chem. Phys. **13**, 15792 (2011).

[5] Y. Oba, N. Watanabe, A. Kouchi, T. Hama, and V. Pirronello, Astrophys. J. Lett. **712**, L174 (2010).

[6] Y. Oba, N. Watanabe, T. Hama, K. Kuwahata, H. Hidaka, and A. Kouchi, Astrophys. J. **749**, 67 (2012).

[7] A. Zangwill, *Physics at Surfaces* (Cambridge University Press, New York, 1988).

[8] R. Gomer, Rep. Prog. Phys. **53**, 917 (1990).

[9] L. J. Lauhon and W. Ho, Phys. Rev. Lett. **85**, 4566 (2000).

[10] C. Laffon, S. Lacombe, F. Bournel, and P. Parent, J. Chem. Phys. **125**, 204714 (2006).

[11] S. Lacombe, F. Bournel, C. Laffon, and P. Parent, Angew. Chem., Int. Ed. **45**, 4159 (2006).

[12] P. Cabral do Couto, R. C. Guedes, B. J. Costa Cabra, and J. A. Martinho Simões, J. Chem. Phys. **119**, 7344 (2003).

[13] K. Tsuji and K. Shibuya, J. Phys. Chem. A **113**, 9945 (2009).

[14] S. Du and J. S. Francisco, J. Phys. Chem. A **112**, 4826 (2008).

[15] W. M. C. Sameera, B. Senevirathne, S. Andersson, F. Maseras, and G. Nyman, J. Phys. Chem. C **121**, 15223 (2017).

[16] T. Hama, K. Kuwahata, N. Watanabe, A. Kouchi, Y. Kimura, T. Chigai, and V. Pirronello, Astrophys. J. **757**, 185 (2012).

[17] K. Kuwahata, T. Hama, A. Kouchi, and N. Watanabe, Phys. Rev. Lett. **115**, 133201 (2015).

[18] K. Kobayashi, J. Phys. Chem. **87**, 4317 (1983).

[19] T. G. Slanger and G. Black, J. Chem. Phys. **77**, 2432 (1982).

[20] G. A. Cruz-Diaz, R. Martín-Doménech, E. Moreno, G. M. Muñoz Caro, and Y.-J. Chen, Mon. Not. R. Astron. Soc. **474**, 3080 (2018).

[21] P. Redondo, F. Pauzat, Y. Ellinger, and A. Markovits, Astron. Astrophys. **638**, A125 (2020).

[22] A. Yabushita, T. Hama, D. Iida, and M. Kawasaki, J. Chem. Phys. **129**, 014709 (2008).

[23] T. Hama, A. Yabushita, M. Yokoyama, M. Kawasaki, and S. Andersson, J. Chem. Phys. **131**, 054508 (2009).

[24] M. Collard, P. Kerwin, and A. Hodgson, Chem. Phys. Lett. **179**, 422 (1991).

[25] PGOPHER VERSION 10.0, C. M. Western, 2017, University of Bristol Research Data Repository, doi:10.5523/bris.160i6ixoo4kir1jxvawfws047m.

[26] M. E. Greenslade, M. I. Lester, D. Č. Radenović, A. J. A. van Roij, and D. H. Parker, J. Chem. Phys. **123**, 074309 (2005).

[27] K. P. Huber and G. Herzberg, *Molecular Spectra and Molecular Structure IV. Constants of Diatomic Molecules* (Van Nostrand Reinhold, New York, 1979).

[28] T. Hama, A. Kouchi, and N. Watanabe, Science **351**, 65 (2016).

[29] T. Hama, M. Yokoyama, A. Yabushita, M. Kawasaki, P. Wickramasinghe, W. Guo, H.-P. Loock, M. N. R. Ashfold, and C. M. Western, J. Chem. Phys. **131**, 224512 (2009).

[30] T. Hama, M. Yokoyama, A. Yabushita, M. Kawasaki, S. Andersson, C. M. Western, M. N. R. Ashfold, R. N. Dixon, and N. Watanabe, J. Chem. Phys. **132**, 164508 (2010).

[31] F. M. Zimmermann and W. Ho, J. Chem. Phys. **100**, 7700 (1994).

[32] E. B. D. Bourdon, P. Das, I. Harrison, J. C. Polanyi, J. Segner, C. D. Stanners, R. J. Williams, and P. A. Young, Faraday Discuss. Chem. Soc. **82**, 343 (1986).

[33] M. Sinvani, P. Taborek, and D. Goodstein, Phys. Lett. A **95**, 59 (1983).

[34] G. A. Kimmel, K. P. Stevenson, Z. Dohnálek, R. S. Smith, and B. D. Kay, J. Chem. Phys. **114**, 5284 (2001).

[35] C. Krischer and D. Lichtman, Phys. Lett. A **44**, 99 (1973).

[36] S. B. King, D. Wegkamp, C. Richter, M. Wolf, and J. Stähler, J. Phys. Chem. C **121**, 7379 (2017).

[37] J. Stähler, J.-C. Deinert, D. Wegkamp, S. Hagen, and M. Wolf, J. Am. Chem. Soc. **137**, 3520 (2015).

[38] W. Hoheisel, K. Jungmann, M. Vollmer, R. Weidenauer, and F. Träger, Phys. Rev. Lett. **60**, 1649 (1988).

[39] I. Lee, T. A. Callcott, and E. T. Arakawa, Anal. Chem. **64**, 476 (1992).

[40] I. Lee, J. E. Parks II, T. A. Callcott, and E. T. Arakawa, Phys. Rev. B **39**, 8012 (1989).

[41] L. W. Chung, W. M. C. Sameera, R. Ramozzi, A. J. Page, M. Hatanaka, G. P. Petrova, T. V. Harris, X. Li, Z. Ke, F. Liu *et al.*, Chem. Rev. **115**, 5678 (2015).

[42] W. M. C. Sameera and F. Maseras, J. Chem. Inf. Model. **58**, 1828 (2018).

[43] M. J. Frisch, G. W. Trucks, H. B. Schlegel, G. E. Scuseria, M. A. Robb, J. R. Cheeseman, G. Scalmani, V. Barone, G. A. Petersson, H. Nakatsuji *et al.* GAUSSIAN 16, Revision A.03 (Gaussian, Inc., Wallingford CT, 2016).

[44] J.-D. Chai and M. Head-Gordon, Phys. Chem. Chem. Phys. **10**, 6615 (2008).

[45] F. Weigend and R. Ahlrichs, Phys. Chem. Chem. Phys. **7**, 3297 (2005).

[46] W. D. Cornell, P. Cieplak, C. I. Bayly, I. R. Gould, K. M. Merz, D. M. Ferguson, D. C. Spelimeyer, T. Fox, J. W. Caldwell, and P. A. Kollman, J. Am. Chem. Soc. **117**, 5179 (1995).

[47] Y. Zhao and D. G. Truhlar, Theor. Chem. Acc. **120**, 215 (2008).

[48] J. Wang and B. Durbeej, J. Comput. Chem. **41**, 1718 (2020).

[49] R. Grotjahn and M. Kaupp, J. Chem. Theory Comput. **16**, 5821 (2020).

[50] J. Gong, J. W. Y. Lam, and B. Z. Tang, Phys. Chem. Chem. Phys. **22**, 18035 (2020).

[51] T. D. Crawford, M. L. Abrams, R. A. King, J. R. Lane, D. P. Schofield, and H. G. Kjaergaard, J. Chem. Phys. **125**, 204302 (2006).

[52] Y. Xie and H. F. Schaefer III, J. Chem. Phys. **98**, 8829 (1993).

[53] C. S. Brauer, G. Sedo, E. M. Grumstrup, K. R. Leopold, M. D. Marshall, and H. O. Leung, Chem. Phys. Lett. **401**, 420 (2005).

[54] M. D. Marshall and M. I. Lester, J. Phys. Chem. B **109**, 8400 (2005).

[55] D. M. Chipman, J. Phys. Chem. A **112**, 13372 (2008).